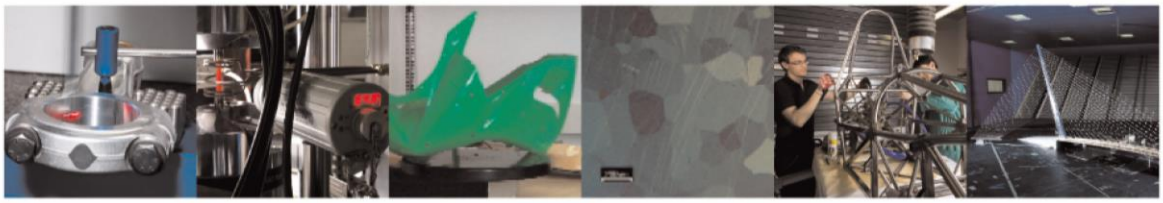

# Limits and solutions in processing pure Cu via selective laser melting using a high-power single-mode fiber laser

Colopi, M.; Demir, A. G.; Caprio, L.; Previtali, B.



DIPARTIMENTO DI MECCANICA ■ POLITECNICO DI MILANO
via G. La Masa, 1 ■ 20156 Milano ■ EMAIL (PEC): pecmecc@cert.polimi.it
http://www.mecc.polimi.it
Rev. 0

# Limits and solutions in processing pure Cu via selective laser melting using a high-power single-mode fiber laser

Matteo Colopi, Ali Gökhan Demir*, Leonardo Caprio, Barbara Previtali

Department of Mechanical Engineering, Politecnico di Milano, Via La Masa 1, 20156 Milan, Italy

*Corresponding author: aligokhan.demir@polimi.it

# Limits and solutions in processing pure Cu via selective laser melting using a high-power single-mode fiber lasers

Matteo Colopi, Ali Gökhan Demir*, Leonardo Caprio, Barbara Previtali

Department of Mechanical Engineering, Politecnico di Milano, Via La Masa 1, 20156 Milan, Italy

*Corresponding author: aligokhan.demir@polimi.it

## Abstract

The demand for additive manufacturing (AM) of Cu and its alloys shows an increased trend from the energy and heat transfer related applications. Selective laser melting (SLM) is amongst the key AM processes for metals, providing high geometrical accuracy and design flexibility. The technology is most commonly employed using high brilliance fiber lasers operating at 1 μm. However, the elevated reflectivity of Cu at this wavelength, combined with its high thermal conductivity is the cause for a highly unstable process, whereby pore-free products are difficult to obtain. Accordingly, the present work explores the limitations in processing pure Cu powders with a 1 kW single mode fiber laser providing solutions and different strategies for improving part quality. In particular, the power level requirements, as well as build plate material, is assessed through an analytical model. Later on, the process parameters were studied for single and multi-pass melting strategies. The results demonstrate that a correct sequence of multi-pass strategy can improve the part density up to 99.1±0.2% with an industrially acceptable build rate of 12.6 $cm^3$/h.

**Keywords:** Pure Cu; porosity; defect correction; multi-pass; selective laser melting

## 1. Introduction

Pure copper is the reference material for thermal and electrical conductivity. Some of the key application sectors are electronics, automotive, aerospace and power production, where the thermal or electrical conductivity efficiency depends not only on material properties, but also on the geometry.

Under this point of view, the combination of the properties of pure copper with the high precision and resolution of selective laser melting (SLM) could potentially enhance the performances of these components. Especially for heat conduction applications, SLM can be employed to generate complex channels for optimized conformal cooling or realise plate-fin heat exchangers avoiding the cost consuming assembly phase[1]. Although the process demonstrates great potential, the use of selective laser melting for the production of pure Cu components has not been widely explored in literature. The reasons behind this lack of investigation are based on the same physicochemical properties which make this metal so desirable for the industry. For instance, the excellent thermal conductivity of pure copper, in combination with its surface tension forces, may easily induce Plateau-Rayleigh instabilities in the molten pool [2]. As a consequence, molten copper tends to contract in spheroidal sections instead of forming a continuous bead, hindering the uniformity of successive layers of powder spreading. In this frame, the solid base plate, utilized as a substrate for the deposition of the initial layers, exerts a crucial influence on the melt pool stability which is fundamental for a successful outcome [3,4]. Another factor determining the absorptivity of the metallic powders is the powder size distribution and powder bed packing density [5,6].

Indeed, application-driven studies have been demonstrated by different groups namely Princeton Plasma Physics Laboratories [7], NASA [8], Daihen [9], Fraunhofer Institute for Laser Technology [10] and 3T-RPD [11]. Industrially, copper alloys are more commonly processed by SLM due to an improved process stability, since they are characterized by a higher absorptivity and lower conductivity with respect to pure copper [12–15]. Concerning the scientific literature, the processing of Cu and its alloys has been treated sparingly. Wang *et al.* showed the SLM of ink-printed Cu nanoparticles for tribological applications [16]. Trevisan *et al.* employed a fiber laser achieving up to 83% part density[17]. Recently, there are indications that the use of high power fiber lasers may be fundamental to improve results. Imai *et al.* employed a high power fiber laser achieveing part density

values up to 96.6%[18]. Colopi *et al.* achieved maximum part density 97.6% with a high level of detail[19]. On the other hand, Jadhav *et al.* combined high power fiber laser with very high energy densities providing conditions which yielded specimens with part densities at 98% range [20]. However, the authors observed severe damage on the laser optics due to back reflection of the laser. The use of shorter wavelength for improved optical absorption is also a possibility under investigation. Fraunhofer ILT [21] and Trumpf [22] have recently demonstrated the use of a high power green solid-state lasers. Masuno *et al.* employed a blue diode laser with a large beam (200 μm) for the SLM of pure Cu [23]. Nonetheless, high power green and blue wavelength lasers with beam sizes suited to SLM are still not widely available.

The present study is aimed at analysing the processability of pure copper by selective laser melting using a 1 kW single mode fiber light source defining the limits, strategies and suitable processing conditions for the production of components. The materials and SLM system employed for the experimental work are presented along with the experimental plans devised for the investigation of the impact of different base plates and of the multi-pass scanning strategies. The thermal field propagation within the base plate was modelled in order to understand the impact of different materials and processing parameters. The results of the experimental analysis are confirmed by the model predictions and a final discussion is exposed.

## 2. Materials and methods

### 2.1. Material

Gas atomized pure copper powder (Cu 99.9%wt, O 0.08%wt, P <0.15%wt) was used throughout the work (LPW Technology Ltd, Runcorn, UK). The powder particle size was 15-45 μm. Fig. 1 shows the SEM image of the powder and the size distribution. Base plate materials were C110 copper (99.9 wt% Cu) and AISI 316L stainless steel (Cr 16-18 wt%, Ni 10-14 wt%, Mo 2-3 wt%, Mn 2 wt%; C

<0.03 wt%, Fe Bal.) [24,25]. The surfaces were prepared by manual roughening using abrasive paper. The average surface roughness values were measured as Ra=2.02±0.14 μm on AISI 316L and Ra=2.41±0.25 μm on C110 base plate. Base plate types are illustrated in Fig.2. The base plate configurations are shown schematically in Fig.3.

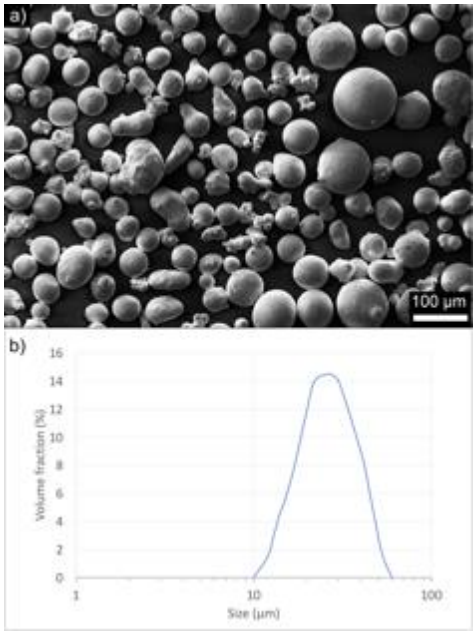


**Fig. 1 a) SEM image, b) size distribution of the 99.9% pure Cu powder**

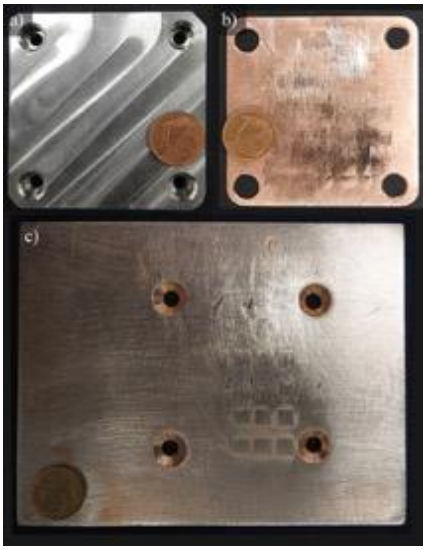


**Fig. 2 Base plate configurations. a) 12 mm thick AISI 316L base plate, b) 1 mm thick C110 mask, c) 5 mm C110 base plate**

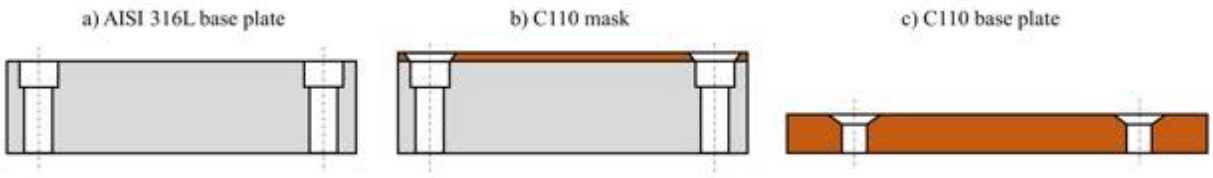


**Fig. 3 Schematic representation of the base plate configurations. a) AISI 316L base plate, b) C110 mask, c) C110 base plate.**

### 2.2. Selective laser melting system

Selective laser melting process was performed employing an open SLM system. This reconfigurable system allows working under inert Ar atmosphere spreading pure Cu powder by means of an automated powder delivery system as previously presented [26,27]. For the present study, the system was equipped with a 1 kW single-mode fiber laser source (*n*LIGHT, Vancouver, WA, USA). This laser source is apt for the processing of highly reflective materials at IR wavelength due to its architecture which is robust against back-reflections, whilst allowing the emission of kilowatt range power. Beam manipulation is guaranteed by a scanner head (Smart Scan SH30G-XY2, Smart Move GmbH, Garching bej München, Germany) coupled with a 75 mm collimating lens and a 420 mm f-theta lens. Consequently, as reported in Tab. 1, the resulting theoretical beam diameter on the focal plane is $d_0 = 78$ µm. The polarisation state of the laser was random.

**Tab. 1 Main characteristics of the open SLM platform *Powderful*** [28]

| Parameter | Value |
|---|---|
| Laser emission wavelength, $\lambda$ (nm) | 1070 |
| Max laser power, $P_{max}$ (W) | 1000 |
| Beam quality factor, $M^2$ | 1.19 |
| Collimating lens, $f_c$ (mm) | 75 |
| Focal lens, $f_{foc}$ (mm) | 420 |
| Nominal beam diameter, $d_0$ (µm) | 78 |
| Build volume (DxWxH), ($mm^3$) | 60x60x20 |

The powder deposition was achieved via a vibrating plate depositing the powder from a hopper, and spread by a rubber wiper. The powder packing was achieved by the translation of the wiper, as no other force was applied perpendicular to the powder bed.

### 2.1. Experimental plan

The experimental work was carried out in two stages concerning single and multi-pass processing conditions. In the single pass strategy study, the influence of base plate material on the part density was the main concern. Once verified the optimal base plate solution, the aim was to understand the most suitable multi-pass scanning strategy to achieve higher density values.

Throughout the work the laser was controlled through a continuous wave (CW) emission profile. The laser emission was turned on at the beginning of each scan vector and turned off at the end. The smallest beam size available was employed, working with the focal point on the powder bed. In this configuration, the beam size is comparable to those available in the industrial SLM systems. No base plate preheating was applied throughout the tests. Ar was employed as a validated inert gas choice in order to avoid any possible effect of affinity with $N_2$ at high temperatures. Prior to the process, vacuum was applied to the build chamber reducing the pressure down to -950 mbar and consecutively flooding with Ar. This procedure was repeated 3 times. During the laser scan period, the gas flow in the inert chamber was maintained with a fan. The process gas was not exchanged throughout the process, since the overall duration and the volume of the scanned specimens were limited. All specimens were built directly on the base plates without support structures. Specimens were cut off from the base plates using a linear saw without any deformation.

#### 2.1.1. Influence of the base plate material

To investigate the impact of the different base plate materials and configurations on the densification of pure Cu components produced by SLM, three alternative solutions were selected: a 12 mm thick

AISI 316L base plate, a 5 mm C110 base plate and a hybrid solution constituted by a 1 mm thick C110 mask overlapped to an AISI 316L base plate. Starting from the feasibility region defined in a previous work [19], an experimental plan has been designed to characterise the density of 5x5x5mm3 cubic samples. Laser power was varied between 600 and 1000 W. To evaluate the influence of hatch distance two levels were experimented, respectively at 70 and 100 μm. Scan speed was varied in a larger interval. For stainless-steel base plate scan speed was varied between 1000 and 3000 mm/s in levels of 500 mm/s, whereas for the C110 base plate and mask the region was extended up to 5500 mm/s in order to test lower energy densities not previously reported in literature. The results were analysed in terms of energy density expressed as:

$$E = \frac{P}{v \cdot h \cdot z} \qquad \textbf{Eq. 1}$$

A single border was scanned for all conditions with the corresponding power and scan speed level. All experiments were carried under Ar atmosphere. Experimental conditions are summarized in Tab. 2.

**Tab. 2 Fixed and varied parameters of the first experimental campaign**

| Fixed parameters | |
|---|---|
| Hatch rotation angle, $\alpha$ (°) | 45 |
| Layer thickness, $z$ (μm) | 50 |
| Process gas | Ar |
| **Varied parameters** | |
| Base plate | AISI316L – C110 base plate – C110 mask |
| Scan speed, $v$ (mm/s) | 1000 - 5500 |
| Laser power, $P$ (W) | 600; 800; 1000 |
| Hatch distance, $h$ (μm) | 70; 100 |

### 2.1.2. Multi-pass strategies

In a second phase of the experimentation, multi-pass scan strategies have been designed and tested on AISI 316L, which was found to be the most performant base plate solution during the single scan study. Multi-pass strategies have been previously employed to remelt at each layer by Demir *et al.* for the processing of 18Ni300 Maraging steel and by Aboulkhair *et al.* working with AlSi10Mg [28–30]. These authors found that part density could be improved by the remelting passes. In this work, the aim of the multi-pass strategy was to stabilize the process by increasing the powder bed temperature gradually and exploit a more efficient melting process due to the increased temperature. A high local temperature difference between the molten pool and the rest of powder bed and solid base plate in its vicinity can act against the processability of pure copper. In fact, strong thermal gradients at the interfaces between the liquid metal and its surroundings induces the balling phenomenon. An increase of the initial temperature in the powder may enhance the process stability. Thanks to the consequent lower and more homogeneous thermal variations, the action of surface tension forces is reduced and, thus the formation of balling instability. Furthermore, an increase of temperature can increase optical absorptivity. Finally, a higher initial temperature corresponds to a lower amount of energy needed to achieve melting due to the reduction of the total gap from the fusion temperature.

Four types of multi-pass strategies have been designed taking as a reference value the energy densities which yielded the highest density specimen in the single-pass experimental campaign (Tab. 3). The different distributions of energy density between two consecutive scans are reported graphically in Fig. 4.

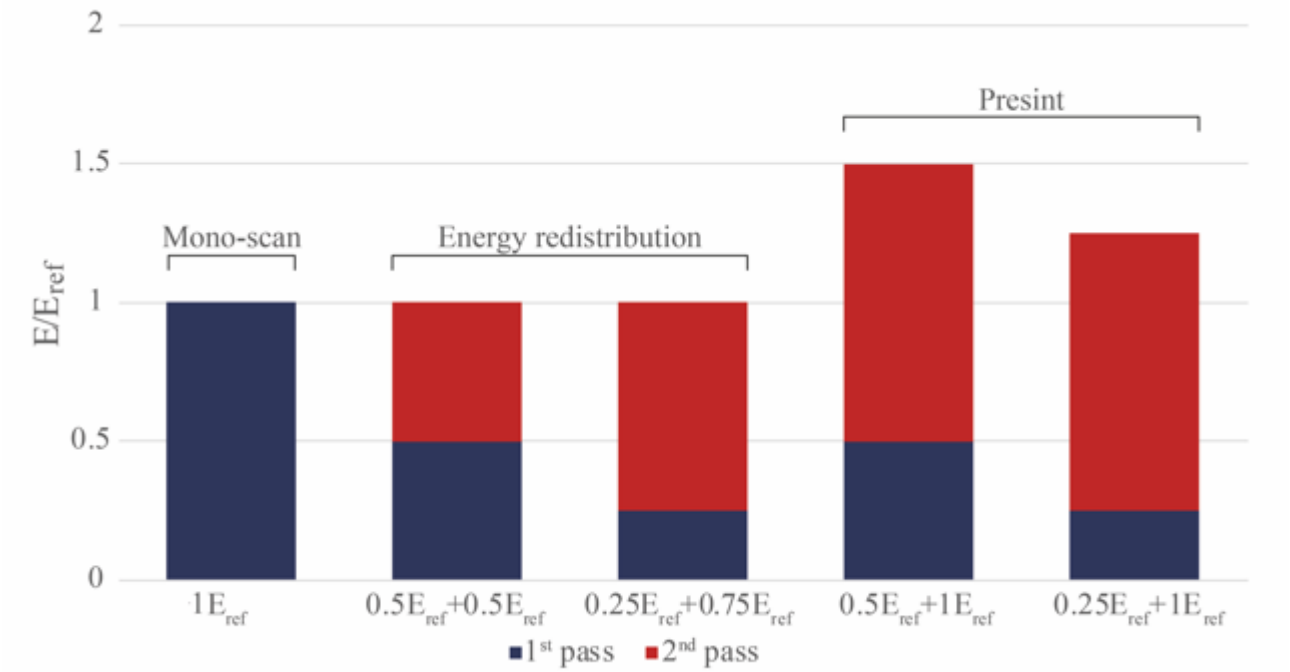


**Fig. 4 Energy density delivered to the powder bed with the different scanning strategies. Energy delivered with the first scan in blue and second scan in red. Values normalized with respect to the reference level, $E_{ref}$**

The spatial disposition of the same energy content was also studied by varying the hatch distance at 40, 70, 100, 130 and 160 μm. In order to keep a constant level of energy density, the hatch variations had to be proportionally compensated by changes in scan speed (using the relation previously defined in Eq.1). Thus, for every level of hatch distance ($h_i$), the correspondent scan speed ($v_i$) has been calculated from the reference energetic density.

$$v_i = P_{ref}/E_{ref}h_i z \qquad \textbf{Eq. 2}$$

Fractions of the reference energy density are, then, obtained variating the laser power between the two consecutive scans.

$$P_i = \eta_i E_{ref} h_i v_i z \qquad \textbf{Eq. 3}$$

where $\eta$ is the fraction used for the layer.

**Tab. 3 Fixed and varied parameters in the experimental campaign for multi-pass strategy study**

| Fixed parameters | |
|---|---|
| Hatch rotation angle, $\alpha$ (°) | 45 |
| Layer thickness, $z$ (µm) | 50 |
| Process gas | Ar |
| Reference energy density, $E_{ref}$ (J/mm3) | 114 |
| Laser power, $P$ (W) | 800 |
| Base plate | AISI316L |

| Varied parameters | |
|---|---|
| Hatch distance, $h$ (µm) | 40; 70; 100; 130; 160 |
| Scan strategy: | |
| Mono-scan | 1 $E_{ref}$ |
| Energy redistribution | 0.5 $E_{ref}$ + 0.5 $E_{ref}$ ; 0.25 $E_{ref}$ + 0.75 $E_{ref}$ |
| Presint | 0.5 $E_{ref}$ + 1 $E_{ref}$ ; 0.25 $E_{ref}$ + 1 $E_{ref}$ |

*Energy redistribution strategies*

The aim of the strategies was to redistribute a reference energy input in two consecutive scans. Two different proportions of energetic input between the first and second scans were considered. The first strategy employed equal distribution between scans (0.5 $E_{ref}$ + 0.5 $E_{ref}$) and the second considered a quarter of the total energy in the first scan and the rest in the second (0.25 $E_{ref}$ + 0.75 $E_{ref}$).

*Presint strategies*

The aim of the presint strategies was to introduce a lower energy input scan prior to the reference one. Hence, the total energy input delivered was higher than the reference. The first scan had the objective of inducing an initial sintering of the powder and thus analyse if such local preconditioning of the surface facilitates optical absorption and a stable melting condition. Two different strategies were tested adding a half (0.5 $E_{ref}$ + 1 $E_{ref}$) and a quarter (0.25 $E_{ref}$ + 1 $E_{ref}$) of the energy input during the first scan. A single border was scanned for each scan pass with the corresponding power and scan speed level.

### 2.2. Characterization

Part density was the main characteristic studied in the present experimental work. Metallographic cross-sections of the specimens were prepared by conventional cutting, mounting, and polishing operations. Images of the cross-section of the entire cubic specimens were taken using optical microscopy (Mitutoyo Quick Vision ELF QV-202). Images were then binarized to calculate the apparent density which was determined as follows:

$$\rho_A = \frac{A_{tot} - A_{pore}}{A_{tot}} \quad \textbf{Eq. 4}$$

where $A_{tot}$ is the total area considered and $A_{pore}$ is the total area of the pores [31]. Each measurement was replicated three times on every section analysed. Border porosity was not analysed as the border scan parameters were not the main subject of this work.

The impact of multi-pass strategies on the productivity of the process has been evaluated calculating the theoretical build rate (*BR*) of the process [28,29]

$$BR = \frac{v}{N} \cdot h \cdot z \quad \textbf{Eq. 5}$$

where *N* is the number of passes.

### 2.3. Results and discussion

#### 2.3.1. Part integrity and apparent density with different base plates

Cubic samples built on different types of base plates are shown in Fig. 7. It can be seen that free-standing samples without macro-defects could be deposited on all the base plate types. On C110 base plate and mask some samples could not be fully processed, which did not necessarily correspond to the lowest energy density conditions. It is expected that the local variations in the optical absorption

behaviour can also play a critical role on the processability of the specimens on the Cu base plate and mask.

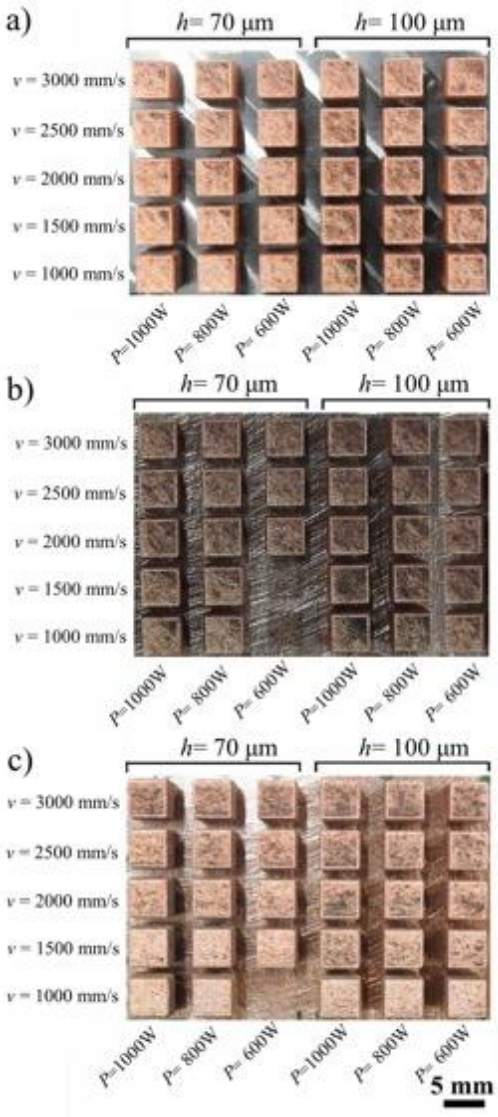


**Fig. 5 Overview of cubic samples built on a) AISI 316L base plate, b) 5 mm thick C110 base plate, c) 1 mm thick C110 mask.**

Fig. 6 shows the apparent density measurements as a function of energy density and base plate material. The apparent densities on stainless steel base plate (Fig. 6.a) showed an increasing trend followed by a stabilization area around a plateau and a successive decay. Similar distributions of densities are common for powder bed fusion samples produced at varying levels of energy density [32,33]. As the energy content delivered increases, the apparent density grows until it stabilizes

around the highest levels achievable and, then, starts to decay again. The main difference in the case of pure Cu is related to the large oscillation band between $\rho_A$= 90% and $\rho_A$=100%. This phenomenon signals an unstable process with very large variations in the part density.

The apparent density of the pure Cu specimens built on the C110 base plate and mask followed a very dispersed behaviour without achieving high values (Fig. 6.b and c). The so-called plateau region appears to be absent with the C110 base plate and mask, where a very large dispersion can be observed. Overall, on both Cu-based base-plates, the highest apparent densities were observed at relatively lower energy densities (approximately 50 J/mm$^3$) with respect to the AISI 316L base plate. An abrupt decay of apparent density can be witnessed with a higher energetic input. Evidently, a constant and stable melt pool is difficult to maintain on C110 base plate and mask due to the high conductivity of the base plate.

Further investigations on the defect morphology were carried out to understand the underlying mechanism for defect formation. Indeed, the predominant pore shape can be an indicator of the defect formation mechanism. Fig. 7 compares the cross-section images of the highest apparent density conditions achieved on the three different base plate types. The highest level of density obtained on AISI 316L base plate corresponded to 98.7% ± 0.2 and the pores are predominantly round. This expresses a condition of vapour or gas entrapment [30,34]. The highest density on the C110 base plate was 90.2%. The pores are large and connected between the layers. This confirms a defect formation mechanism also based on the delamination of loosely adhered regions during the process. Under the influence of the thermal stresses generated, the scanned layer may detach from the previously deposited layers [35]. The highest density on C110 mask was 98.6%. The pores were fragmented, which suggests a lack-of-fusion defect formation mechanism.

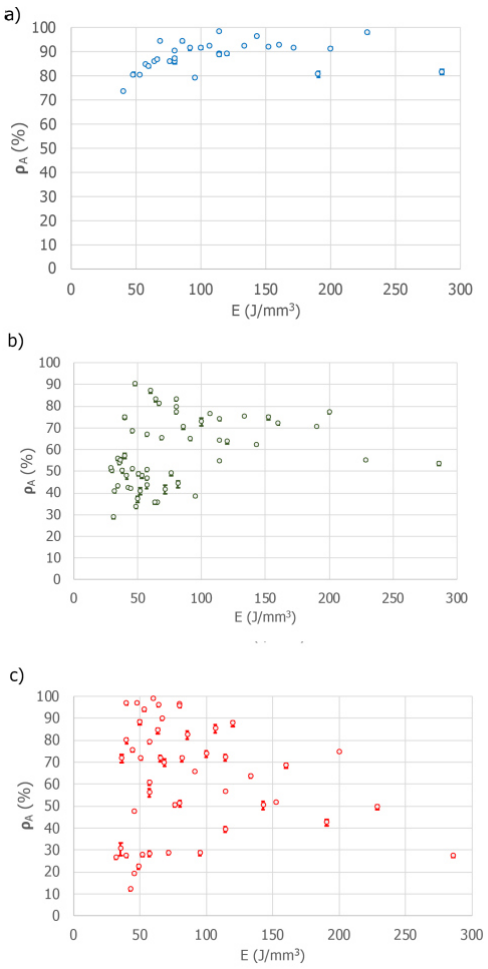


**Fig. 6 Mean apparent density $\rho_A$ of pure Cu deposited on (a) AISI 316L, (b) C110 base plate and (c) C110 mask. Error bars represent the standard deviation of the measurements**

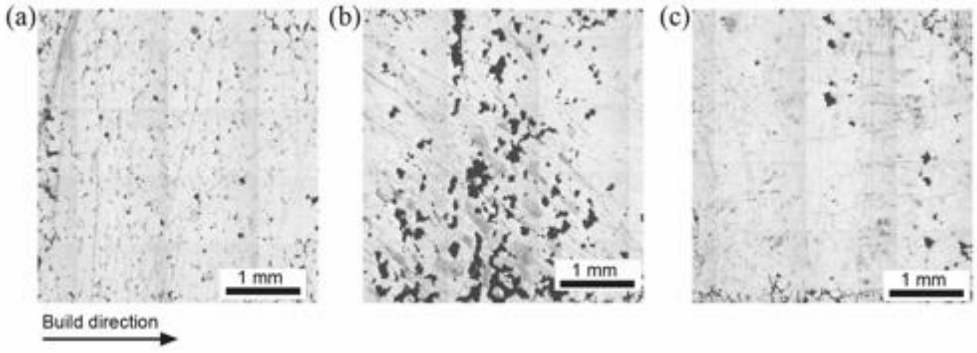


**Fig. 7 Cross-sections of specimens with the highest measured density on different base plates: (a) AISI 316L ($\rho_A$ = 98.7% ± 0.2; E= 114 J/mm3), (b) C110 base plate ($\rho_A$ = 90.2% ± 0.7; E= 48 J/mm3), (c) C110 mask ($\rho_A$ = 98.6% ± 0.2; E= 60 J/mm3).**

The overall conclusion is that the use of an AISI 316L base plate is more suitable for a stable SLM process of pure Cu powders. The use of a C110 mask compared to the C110 base plate shows to slightly improve the densification behaviour owing to a decrease of the overall thermal conductivity. However, both the C110 base plate and mask solutions do not provide a sufficiently stable processing condition for pure Cu.

### 2.3.2. Apparent density with multi-pass strategies

Fig. 8 reports the measured apparent density values as a function of the scan strategies and hatch distance. It can be seen that enlarging the hatch distance with the Mono-scan strategy generated a notable reduction in density (Fig. 8.a). Evidently, the slower scan speed used to maintain the same energy density did not compensate the melt pool size in order to fill the gap between the hatch lines [36]. An abrupt decrease of apparent density was observed when employing values above of hatch distance 100 µm, suggesting that complete separation of melt pool tracks occurs above this value. A hatch distance of 70 µm appeared to be the most suitable, while further reduction showed a slight decrease of apparent density. It can be expected that with 40 µm hatch distance, the scan speed increase may reduce the apparent density due to the reduced interaction time over the scanned line [37,38].

Overall, the multi-pass scan strategies appeared to be less prone to a decay in the apparent density as a function of the hatch distance. Compared to the mono-scan strategy, an improvement of the apparent density wass possible through the energy redistribution strategies, while the presint strategies did not provide conditions with apparent density values above 99% (Fig. 8.b and c). Results show that both the temporal disposition as well as the amount of energy delivered to the powder bed are important in determining the densification conditions. Both the energy redistribution and presint strategies, show that the use of 0.5 $E_{ref}$ during the first pass yields higher density results. It can thus be expected

that after a scanning with 0.5 $E_{ref}$, the surface temperature and powder bed compactness are in the optimal condition to receive a second pass to achieve full melting. This may be due to the higher optical absorption which hence allow for a greater process efficiency. It should be noted that the energy redistribution strategy delivers a lower input with respect to the presint strategy (see Fig. 4). Apparent densities are overall higher for the energy redistribution strategy hence implying that an excessive energetic input in the second pass is detrimental for the process outcome.

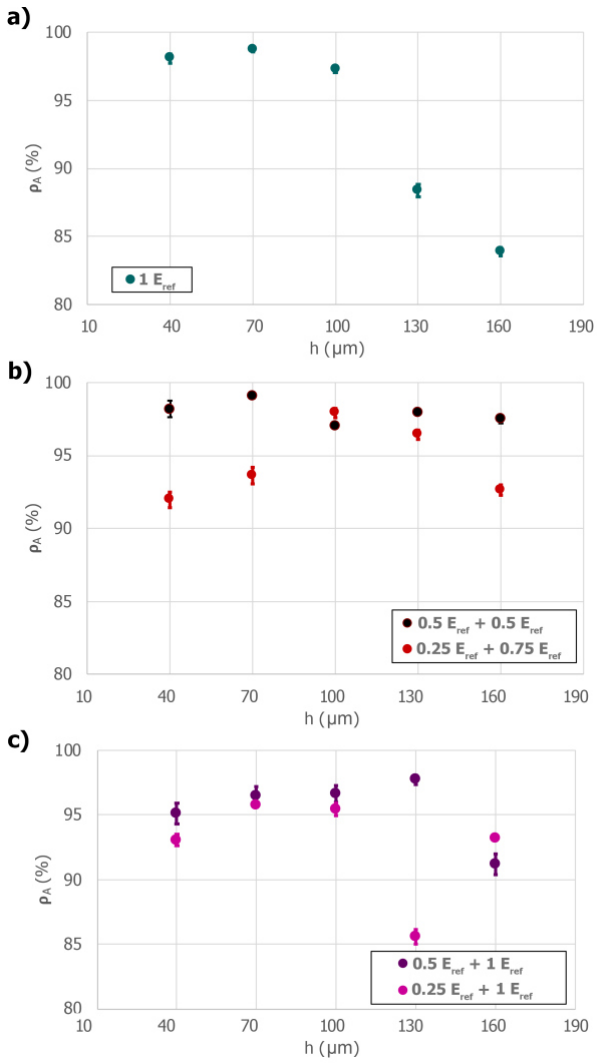


**Fig. 8 Apparent density as a function of hatch distance and scan strategy. a) Mono-scan, b) energy redistribution, c) presint. Error bars represent standard deviation of the measurements.**

The spatial disposition of the energy input was also an important influencing factor of the multi-pass strategies. The optimal hatch distance level varied for the different multi-pass strategies, implying a strong interaction between the process parameters. The highest apparent density value ($\rho_A$=99.1%) was obtained employing the energy redistribution strategy 0.5 $E_{ref}$ + 0.5 $E_{ref}$ and $h$=70 μm. On the other hand, when employing the mono-scan strategy, the highest apparent density value attested itself at $\rho_A$=98.7% employing a hatch distance of $h$= 70 μm. It may be thus inferred that the use of the same energetic input in two successive scans positively affects the process outcome in terms of the obtainable apparent density.

Fig. 9 reports the images of the metallographic cross-sections of the samples with the highest apparent density for each of the different scan strategies. It can be observed that the pore size and morphology changes also in this case. As previously stated, the highest density was achieved with the 0.5 $E_{ref}$ + 0.5 $E_{ref}$ energy redistribution strategy. In this condition, the pores were smaller compared to the mono-scan and more dispersed, showing effects of gas entrapment. The 0.25 $E_{ref}$ + 0.75 $E_{ref}$ energy redistribution strategy instead shows signs of lack of fusion with larger pores that are irregular in shape. Same observations can be made of the presint samples. Where lower values of apparent density are reported (for 0.5 $E_{ref}$ + 1 $E_{ref}$ and 0.25 $E_{ref}$ + 1 $E_{ref}$), the pores connected between scan lines and layers.

The build rates calculated for the different scan strategies are shown in Tab. 4. It is evident how the use of multiple passes significantly reduces the productivity from 25.2 $cm^3$/h to 12.6 $cm^3$/h. Due to the parametric compensation of the power and scan speed levels, the change in energy level and hatch distance does not influence the build rates. Even though multiple passes are required to obtain elevated values of apparent density, the build rates are comparable to those of more conventional materials such as AISI316L and 18Ni300 steels (this is an advantage of using a high power fiber laser) [28,39].

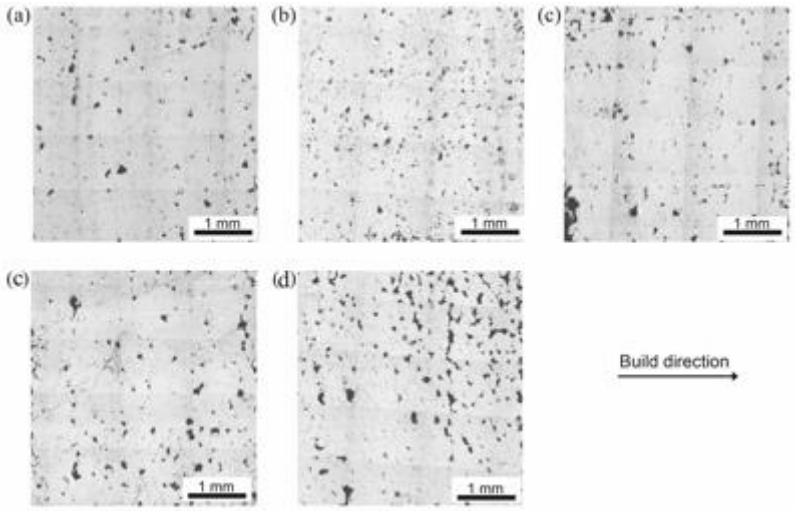


**Fig. 9 Cross sections of specimens with the highest mean density for different strategies. (a) Mono-scan strategy ($\rho_A$ = 98.7% ± 0.2; h = 70 µm). Energy redistribution strategies: (b) 0.5 $E_{ref}$ + 0.5 $E_{ref}$ ($\rho_A$ = 99.1% ± 0.2; h = 70 µm) and (c) 0.25 $E_{ref}$ + 0.75 $E_{ref}$ ($\rho_A$ = 97.9% ± 0.3; h = 100 µm). Presint strategies: (c) 0.5 $E_{ref}$ + 1 $E_{ref}$ ($\rho_A$ = 97.7% ± 0.3; h = 130 µm), (d) 0.25 $E_{ref}$ + 1 $E_{ref}$ ($\rho_A$ = 95.8% ± 0.2; h = 70 µm). Build direction corresponds to the horizontal plane in the images.**

**Tab. 4 Calculated build rate for every scan strategy**

| **Strategy** | **Mono-scan** | **Energy redistribution** | **Presint** |
|---|---|---|---|
| *BR* ($cm^3$/h) | 25.2 | 12.6 | 12.6 |

The results of the present research show how a high power fiber laser is a viable option for the SLM processing of pure Cu. However, it should be noted that the optical chain undergoes an important amount of thermal stress due to the high power and elevated amount of back reflected laser light. From this point of view, the multi-pass strategies can also be advantageous as they reduce the emitted power per pass with respect to a mono-scan pass strategy. Another important point is related to the processing of larger components and therefore scanned layers. A constant powder bed temperature can play a critical role on process stability. Therefore, different scan patterns (*e.g.* chess-board, stripes) might be required for larger parts.

## 3. Analytical modelling of the thermal field with different base plate materials as an aid for process comprehension

Analytical models have been effectively used to model the temperature fields in laser based melting processes. The mathematical solution for a moving point source model was derived for first by Carlsaw and Jaeger [40] while its first application to manufacturing was by Rosenthal for the welding process [41,42]. Other applications of moving heat source solutions may be found in the work by Van Elsen *et al.* [43], whereby the authors developed an analytical solution to be used in laser based fusion processes employing point, ellipsoidal and uniform heat distributions. The authors discussed the effect of different process parameters, as well as heat source selection on the results of the simulations, declaring the efficacy of analytical solutions to estimate the processing conditions. Tan *et al.* [44] employed an analytical solution for laser metal deposition to calculate the thermal field and the deposit geometry. The authors employed a moving square heat source over a single line. The work uses analytical modelling for a better comprehension of the process dynamics, once an opportune calibration stage had been applied. Ning *et al.* [45] applied a moving heat source to the SLM process considering latent heat of fusion and optical absorption of the material. The authors underlined the influence of powder packing density on the melt pool geometry due to the change of the optical absorption. Caprio *et al.* [38] on the other hand investigated the effect of the laser temporal emission profile in selective laser melting by employing a moving Gaussian heat source. The presence of the thin powder layer over the base plate material was modelled using the method of images to achieve more accurate solutions. The authors employed the analytical model to estimate the melting process efficiency. Overall, analytical models provide a compromise between a fast solution and acceptable accuracy [46]. Accordingly, the complexity of the model and its solution must be tailored. In this work, an analytical solution based on an apparent spot formed over the whole scanned region is employed. The solution is used for a better comprehension of the processing condition, especially

concerning the base plate influence, which appears to be neglected in the literature overall. A simplified analytical model for understanding the main differences in terms of the thermal field formed during the process as a function of the base plate is thus presented. The problem formulation is made in terms of a stationary heat source. Previous application of such models to study the heat transfer in melting processes may be found in the work by Gellert and Egli and as well as in the reference books for the analytical modelling of laser based processes by Dowden and by Steen and Mazumder [47–49].

Concerning the SLM processing of pure Cu the temperature distribution plays a crucial role for the process stability, since the optical absorption of copper is not only dependent on the wavelength of the incident radiation, but also on the temperature of the material (see Fig.1) [50]. Considering this, it is easy to understand that the energy transfer from the heat source to pure Cu continuously evolves during the process because of temperature variations and material state change, with direct consequences on the laser absorption. This hampers the processability of pure copper in SLM because along a scan line an irregular amount of energy is absorbed by the material.

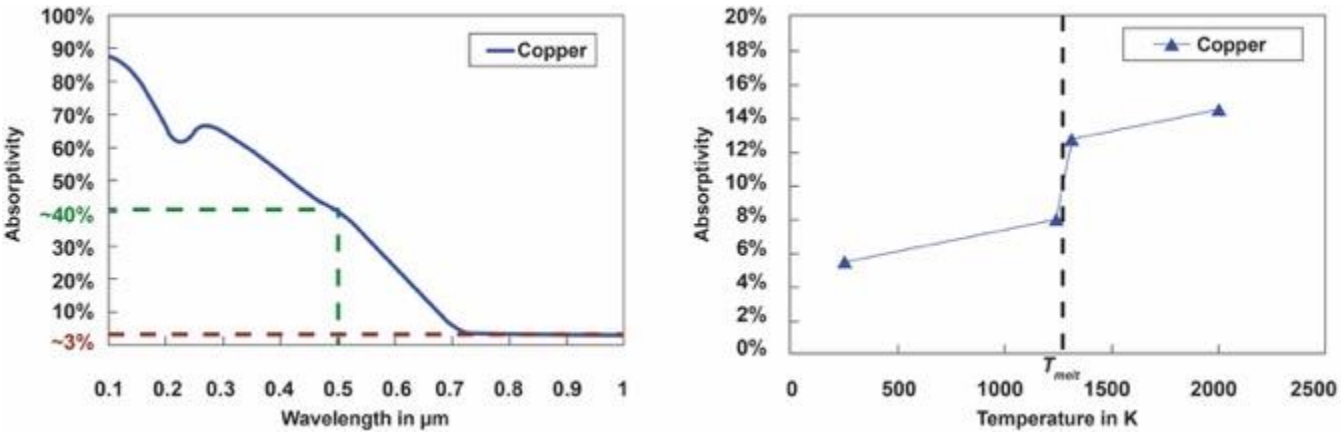


**Fig. 10 Variation of pure Cu as a function of wavelength and temperature (adapted from** [50])

Processability of this metal via SLM with near infrared (NIR) lasers can thus be enforced by exploiting its non-linear optical absorption behaviour. Evidently, the process is required to reach the

molten phase rapidly without dissipating energy to the powder bed and base plate. Under this point of view the use of a high power laser beam and the opportune selection of the solid base plate material are crucial aspects.

Commonly, in selective laser melting the powder and base plate are from the same material family. Alternatively, a base plate material is chosen from a metallurgically compatible alloy to ensure a strong welding of the initial layers to the solid base. In this case, a solid copper base plate could show a significantly higher tendency to dissipate energy from the melt pool since solid bulk metals are more conductive than their correspondent powder forms. Contrarily, if a less conductive metal such as stainless steel is chosen for the base plate, it could behave as a thermal barrier favouring thermal energy concentration near the laser interaction point. The drawback of choosing a base plate made of a material different from pure copper may be welding incompatibility that could lead to structural fragility.

In the perspective of avoiding compatibility problems, whilst limiting heat propagation towards the base plate, the hybrid solution may be considered. A material discontinuity can be introduced by overlapping a copper mask over the stainless steel base plate thus exploiting the thermal conductivity difference of these two metals.

To understand the impact of base plates with different conductivities on the process as well as the effect of laser power variations at fixed levels of energy density, the interaction of a heat source acting directly on the base plate was modelled starting from the mono-dimensional heat conduction equation[40,42,47]:

$$\frac{\partial^2 T}{\partial z^2} = \frac{1}{\alpha}\frac{\partial T}{\partial t} \qquad \textbf{Eq. 6}$$

with $T$ is the base plate temperature, $z$ the vertical coordinate pointing in the base plate from the surface, $t$ stands for time instant and α for thermal diffusivity of the material. The model is valid under the hypothesis of a homogeneous isotropic material, thermal and physical properties constancy, semi-infinite base plate, constant initial temperature ($T_i$) and neglecting phase changes and the effects of convection and radiation. Moreover, the laser is considered to be moving fast on a square area and the exposure time for every point in this region is very small as in the case of the experimental campaign previously presented. Hence, it is possible to approximate from a modelling perspective that each single point is scanned at the same time for a duration equal to the scanning time of the overall resulting apparent spot ($t_{on}$):

$$t_{on} = \frac{l^2}{h * v} \quad \textbf{Eq. 7}$$

where $l$ corresponds to the side of the square apparent spot considered, $h$ the hatch distance and $v$ the scanning speed. It is also possible to define the equivalent heat flow $q_0''$ entering the domain as:

$$q_0'' = \frac{P}{l^2} \quad \textbf{Eq. 8}$$

where $P$ is the laser power and $l$ always the side of the apparent spot size. The modelled thermal field was an approximation to an apparent spot formed all around the scanned region [51]. This approximation can be indeed inadequate for estimating the temperature field over a scanned line, whereas it was deemed adequate for showing the differences between the thermal properties of the base plate materials.

Boundary conditions imposed are such that, at $t = 0$, every point in the semi-infinite base plate is at the initial temperature (Eq. 9). Furthermore, the temperature of the base plate at infinity of the spatial

domain will remain untouched with respect to its initial value. (Eq. 10). Finally, the heat flow is considered acting on the surface and equal to $q_0$'' (Eq. 11).

$$T(z,0) = T_i \quad \textbf{Eq. 9}$$

$$T(\infty,t) = T_i \quad \textbf{Eq. 10}$$

$$-k\left.\frac{dT}{dz}\right|_{z=0} = q_0'' \quad \textbf{Eq. 11}$$

The solution to the heat conduction equation [51] is:

$$T(z,t) - T_i = \frac{q_0''\sqrt{4\alpha t}}{k} ierfc\left(\frac{z}{\sqrt{4\alpha t}}\right) \quad \textbf{Eq. 12}$$

where *ierfc* refers to the integral of the complementary error function. This solution is valid until the heat source is acting on the base plate. Once the thermal energy supplied is interrupted at the instant $t_{on}$, the solution must be modified to account for the cooling action of the bulk base plate:

$$T(z,t) - T_i = \frac{q_0''\sqrt{4\alpha(t_{on}-t)}}{k} ierfc\left(\frac{z}{\sqrt{4\alpha(t_{on}-t)}}\right) \quad \textbf{Eq. 13}$$

In order to compare the C110 and AISI 316L base plate solutions with the hybrid solution of the C110 mask within the same modelling frame, the latter was simulated by applying the "method of images" [52]. It is possible to consider the material discontinuity at the interface between stainless steel and the copper mask as an adiabatic surface due to the elevated difference in thermal conductivity between these two metals, which is of an order of magnitude. The analytical solution was calculated taking the original one, resulting from the model exposed above, and adding to this the same solution reflected alternatively in $z = 0$ and $z = h$. The reflection should be iterated infinite times for a

mathematically exact solution. Computationally, the solution increment becomes negligible after a number of reflections due to the convergence to $T_i$ of the original solution to the mono dimensional heat equation. The expression obtained for the temperature distribution in the range $0 \leq z \leq$ h can be formulated as:

$$T(z,t) - T_{in} = S(z,t) + \sum_{n=-\infty}^{+\infty} S(z - 2nh, t) \qquad \textbf{Eq. 14}$$

where *S(z,t)* is the solution resulting from the model utilized also for the other two base plates and the rest is the superimposition of solutions of this model calculated with $z = 0$ and $z = h$ alternatively for $n$ times. To model the copper mask, a thickness of 1 mm was considered and the analytical solution was reflected 5 times. Process parameters considered for the calculations are reported in Tab. 5. The power input is accounted as acting on a 5 x 5 $mm^2$ square region considering that the points in the region are scanned contemporarily.

**Tab. 5 Parameters utilized in the analytical model** [24,25]

| **Process parameter** | | **Value** |
|---|---|---|
| Scan speed, $v$ (mm/s) | | 2000 |
| Hatch distance, $h$ (μm) | | 70 |
| Laser power, $P$ (W) | | 800 |
| Total exposure time, $t_{on}$ (s) | | 0.179 |
| Initial temperature, $T_i$ (°C) | | 25 |
| | **Cu** | **AISI 316L** |
| Density, $\rho$ ($kg/m^3$) | 7190 | 8936 |
| Heat capacity, $C_p$ ($J/(kg \cdot K)$) | 510 | 380 |
| Thermal conductivity, $k$ (W/(m·K)) | 14 | 385 |
| Heat diffusivity $\alpha$ ($m^2/s$) | $3.443 \cdot 10^{-6}$ | $1.134 \cdot 10^{-4}$ |

Similarly to what has been assumed by Singh *et al*. and Franco *et al*. in their works [53,54], this model does not consider the presence of powder on top of the base plates, neither its implications on the

amount of energy effectively reaching the base plate surface. It is intended as a tool to understand how a heat input, corresponding to the one produced in the previous experimental campaigns for the SLM of pure copper, can distribute in depth and how the thermal field evolves with the different base plate configurations. Although punctual values of temperature may be affected by the neglection of phase changes, the presence of powder and other heat exchange modalities, the curves obtained allow for a prediction of the process behaviour with the different base plate solutions.

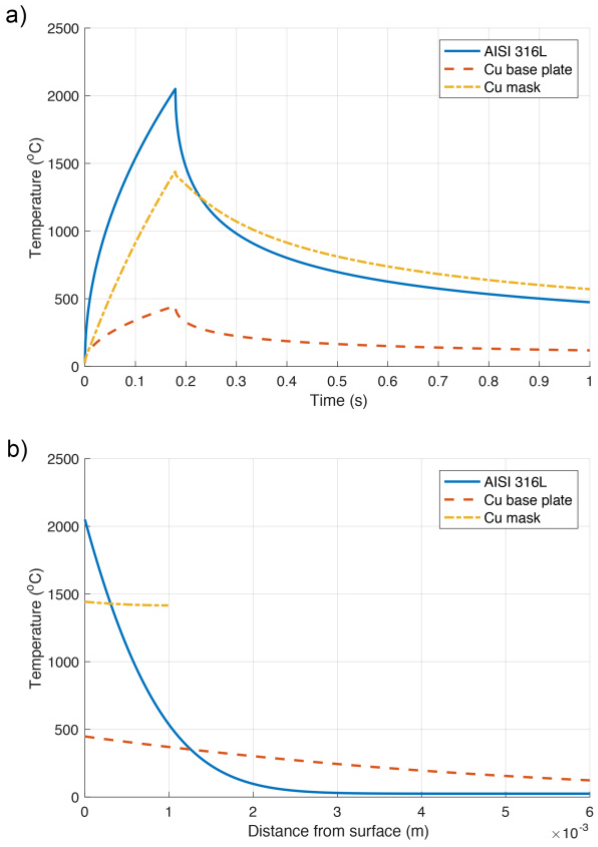


**Fig. 11 (a) Simulated temporal variation of temperature on the surface of the base plate (z = 0 mm) (b) Simulated spatial temperature distribution with 800 W power at t = $t_{on}$.**

Fig. 11. shows the trends calculated with an instantaneous emission power of 800 W. It can be seen that higher peak temperatures are achieved on the surface using the copper mask solution with respect to the C110 base plate (Fig. 11.b). The heat accumulated in 1 mm of depth, at equal heat flux and exposure time, is remarkably stronger. In the C110 mask solution, the cooling phase is slower with

respect to the copper base plate condition testifying a more significant restraint of the heat introduced in the region near the top surface. Besides, the thermal field propagation inside the base plate depth is attenuated differently in the three solutions considered (Fig. 11.a): the highest temperature simulated belongs to the stainless steel base plate, while heat can travel more rapidly through a copper bulk plate impeding a strong accumulation of thermal energy near the powder layer.

The modelling approach explained above has been also utilized to simulate, on the three base plates, the effects of power ($P$) variations on the maximum temperature achievable at a fixed energy input ($E_{tot}$) level with a NIR laser, as defined in Eq. 15.

$$E_{tot} = q'' \cdot t_{on} = \frac{P}{h \cdot v} \qquad \textbf{Eq. 15}$$

The interaction between the heat source accounting for the laser process and the different base plates has been modelled with levels of power typically employed for the SLM process (200-1000W). Keeping the hatch distance fixed, the scan speed has been regulated accordingly to maintain a constant energy input.

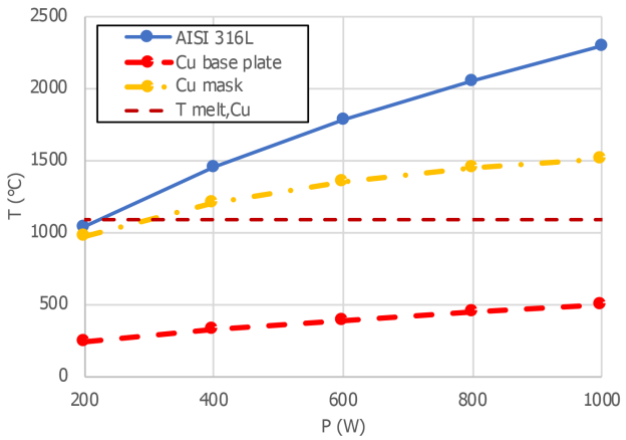


**Fig. 12 Trends of the maximum simulated temperature at different levels of power and base plate materials.**

The maximum temperature plot shown in Fig. 12 puts into evidence that the use of high power and high scan speed is more feasible with respect to a low power, low scan speed combination resulting in the same energy input, which confirms the importance of the high power single mode fiber laser. The influence of the base plate material remains crucial for acting as a thermal barrier indicating that AISI 316L is the more suitable choice, as confirmed by the experimental results.

## 4. Conclusions

In this work, the influence of base plate material and scan strategies with a high power single mode fiber laser on the densification behaviour of highly reflective pure Cu powder was studied. Experimental analyses and analytical modelling were carried out to assess the porosity levels as well as to indicate the underlying mechanism. The main results can be summarized as:

- The use of a high power and high brilliance fiber laser is fundamental to overcome the melting temperature of the highly reflective pure Cu. The non-linear absorption behaviour of Cu at elevated temperatures can be exploited to maintain a stable process.
- The base plate type and its thermal conductivity play a crucial role on maintaining the powder bed temperature and hence the process stability. The use of C110 is problematic due to the very high thermal conductivity. Reduction of the base plate thickness to reduce the heat transfer is influential, but not effective. The use of a stainless steel base plate provides thermal stability due to the reduced thermal conductivity.
- The use of multi-pass strategies significantly improves the apparent density of pure Cu samples. The release of the energetic input should be carefully addressed both in temporal and spatial terms. It was found out that the 114 J/cm$_3$ energy density divided into a energy redistribution strategy with two equal passes, with half the laser power at each pass, improves the apparent density from 98.7±0.2% to 99.1±0.2%.

- The build rates obtained with multiple scan passes are 12.6 $cm^3/h$, comparable to the industrial practice for conventional SLM materials. This is a consequence of the adoption of a reasonable layer thickness at 50 μm and the possibility of employing high scan speeds thanks to laser power levels between 800-1000 W.
- The analytical model confirms that high power-high scan speed combinations along with a base plate with lower conductivity are advantageous for maintaining a stable process.

The present results showed that the SLM processing of pure Cu requires careful adjustment of process parameters throughout the build. Further investigations have to be carried out in order to establish selective laser melting as an industrially reliable technology for the deposition of pure copper. Future works will address resultant electrical and thermal properties of the produced specimen.

**Acknowledgements**

The authors wish to express their gratitude to Optoprim Srl and nLIGHT Inc for their collaboration and technical support. This work was supported by European Union, Repubblica Italiana, Regione Lombardia and FESR for the project MADE4LO under the call "POR FESR 2014-2020 ASSE I - AZIONE I.1.B.1.3".

## References


[1] Raffaelli D, Demir AG, Colombo P, Previtali B, Guagliano M. A study on selective laser melting (SLM) to produce a compact motorcycle heat exchanger. Int. Conf. Innov. Des. Manuf. ICIDM2017, 2017, p. 1–5.

[2] Yadroitsev I, Gusarov A, Yadroitsava I, Smurov I. Single track formation in selective laser melting of metal powders. J Mater Process Technol 2010;210:1624–31. doi:10.1016/j.jmatprotec.2010.05.010.

[3] Liu ZH, Zhang DQ, Sing SL, Chua CK, Loh LE. Interfacial characterization of SLM parts in multi-material processing: Metallurgical diffusion between 316L stainless steel and C18400 copper alloy. Mater Charact 2014;94:116–25.

[4] Sciammarella F, Gonser MJ, Styrcula M. Laser Additive Manufacturing of Pure Copper. Rapid 2013 2013.

[5] Boley CD, Khairallah SA, Rubenchik AM. Calculation of laser absorption by metal powders in additive manufacturing. Addit Manuf Handb Prod Dev Def Ind 2017;54:507–17. doi:10.1201/9781315119106.

[6] Streek A, Regenfuss P, Exner H. Fundamentals of energy conversion and dissipation in powder layers during laser micro sintering. Phys Procedia 2013;41:858–69. doi:10.1016/j.phpro.2013.03.159.

[7] Mendoza HR. Princeton Plasma Physics Laboratory Uses 3D Printing to Produce Parts for Microwave Launchers 2014.

[8] McMahan T. NASA 3-D Prints First Full-Scale Copper Rocket Engine Part n.d.;2017.

[9] Daihen. Daihen establishes copper-alloy 3D additive manufacturing technology using a conventional metal 3D printer n.d.;2016.

[10] für Lasertechnik ILT F-I. Rapid Heat Dissipation from Critical Areas of Injection Molds n.d.;2011.

[11] Burnip S. 3T announces success with Pure Copper production – and an open invitation 2014.

[12] Mao Z, Zhang DZ, Wei P, Zhang K. Manufacturing Feasibility and Forming Properties of Cu-4Sn in Selective Laser Melting. Materials (Basel) 2017;10:333.

[13] Grez JAR, Bourell DL. Solidification Morphology Analysis of SLM of Cu Powder n.d.

[14] Sabelle M, Walczak M, Ramos-Grez J. Scanning pattern angle effect on the resulting properties of selective laser sintered monolayers of Cu-Sn-Ni powder. Opt Lasers Eng 2018;100:1–8.

[15] Pogson SR, Fox P, Sutcliffe CJ, O'Neill W. The production of copper parts using DMLR. Rapid Prototyp J 2003;9:334–43. doi:10.1108/13552540310502239.

[16] Wang X, Liu J, Wang Y, Fu Y. Fabrication of friction-reducing texture surface by selective laser melting of ink-printed (SLM-IP) copper (Cu) nanoparticles (NPs). Appl Surf Sci 2017;396:659–64.

[17] Trevisan F, Calignano F, Lorusso M, Manfredi D, Fino P. Selective laser melting of chemical pure copper powders. Euro PM 2017, Milan: 2017.

[18] Trevisan F, Calignano F, Lorusso M, Lombardi M, Manfredi D, Fino P. Selective laser melting of chemical pure copper powders. Euro PM 2017, 2017, p. 1–6. doi:10.1007/s11837-017-2695-x.

[19] Colopi M, Caprio L, Demir AG, Previtali B. Selective laser melting of pure Cu with a 1 kW single mode fiber laser. Procedia CIRP 2018;74:59–63. doi:10.1016/J.PROCIR.2018.08.030.

[20] Jadhav SD, Dadbakhsh S, Goossens L, Kruth J-P, Van Humbeeck J, Vanmeensel K. Influence of selective laser melting process parameters on texture evolution in pure copper - Manuscript submitted for publication. J Mater Process Technol 2019;270:47–58. doi:10.1016/j.jmatprotec.2019.02.022.

[21] Fraunhofer ILT. Green Light for New 3D Printing Process 2017. https://www.ilt.fraunhofer.de/en/press/press-releases/press-release-2017/press-release-2017-08-30.html.

[22] Trumpf. World premiere at Formnext: green laser from TRUMPF prints copper and gold 2018. https://www.trumpf.com/it_IT/impresa/stampa/comunicatistampa/comunicato-stampa-pagina-con-i-dettagli/release/world-premiere-at-formnext-green-laser-from-trumpf-prints-copper-and-gold/.

[23] Masuno S, Tsukamoto M, Tojo K, Keita; A, Funada Y, Yu S. Metal powder bed fusion additive manufacturing with 100 W blue diode laser. 36th Int Congr Appl Lasers Electro-Optics ICALEO 2017:4–5.

[24] Washko S.D., Aggen G. Wrought Stainless Steels. ASM Handbook, Vol. 1, ASM International; 1990, p. 841–907.

[25] CES EduPack 2017.

[26] Caprio L, Demir AG, Previtali B. Comparative study between CW and PW emissions in selective laser melting. J Laser Appl 2018;30:032305. doi:10.2351/1.5040631.

[27] Demir AG, Monguzzi L, Previtali B. Selective laser melting of pure Zn with high density for biodegradable implant manufacturing. Addit Manuf 2017;15:20–8. doi:10.1016/j.addma.2017.03.004.

[28] Demir AG, De Giorgi C, Previtali B. Design and implementation of a multi-sensor coaxial monitoring system with correction strategies for selective laser melting of a maraging steel. J Manuf Sci Eng 2017;140:1–14. doi:10.1115/1.4038568.

[29] Demir AG, Previtali B. Investigation of remelting and preheating in SLM of 18Ni300 maraging steel as corrective and preventive measures for porosity reduction. Int J Adv Manuf Technol 2017;93:1–13. doi:10.1007/s00170-017-0697-z.

[30] Aboulkhair NT, Everitt NM, Ashcroft I, Tuck C. Reducing porosity in AlSi10Mg parts processed by selective laser melting. Addit Manuf 2014;1:77–86. doi:10.1016/j.addma.2014.08.001.

[31] Spierings AB, Schneider M, Eggenberger R. Comparison of density measurement techniques for additive manufactured metallic parts. Rapid Prototyp J 2011;17:380–6. doi:10.1108/13552541111156504.

[32] Morgan R, Sutcliffe CJ, O'Neill W. Density analysis of direct metal laser re-melted 316L stainless steel cubic primitives. J Mater Sci 2004;39:1195–205. doi:10.1023/B:JMSC.0000013875.62536.fa.

[33] Wang D, Liu Y, Yang Y, Xiao D. Theoretical and experimental study on surface roughness of 316L

stainless steel metal parts obtained through selective laser melting. Rapid Prototyp J 2016;22:706–16. doi:10.1108/RPJ-06-2015-0078.

[34] Kasperovich G, Haubrich J, Gussone J, Requena G. Correlation between porosity and processing parameters in TiAl6V4 produced by selective laser melting. Mater Des 2016;105:160–70. doi:10.1016/j.matdes.2016.05.070.

[35] Van Humbeeck J, Buls S, Thijs L, Kempen K, Vrancken B, Kruth J-P. Selective Laser Melting of Crack-Free High Density M2 High Speed Steel Parts by Baseplate Preheating. J Manuf Sci Eng 2014;136:061026. doi:10.1115/1.4028513.

[36] Gong H, Rafi K, Gu H, Starr T, Stucker B. Analysis of defect generation in Ti-6Al-4V parts made using powder bed fusion additive manufacturing processes. Addit Manuf 2014;1:87–98. doi:10.1016/j.addma.2014.08.002.

[37] Assuncao E, Williams S, Yapp D. Interaction time and beam diameter effects on the conduction mode limit. Opt Lasers Eng 2012;50:823–8. doi:10.1016/j.optlaseng.2012.02.001.

[38] Caprio L, Demir AG, Previtali B. Influence of pulsed and continuous wave emission on melting efficiency in selective laser melting. J Mater Process Tech 2018;266:429–41. doi:10.1016/j.jmatprotec.2018.11.019.

[39] Previtali B, Demir AG, Bucconi M, Crosato A, Penasa M. Comparative costs of additive manufacturing vs. machining: the case study of the production of forming dies for tube bending. Solid Free Fabr Symp 2017:2816–34.

[40] Carslaw HS, Jaeger JC. Conduction of heat in solids. Clarendon Press; 1960.

[41] Rosenthal D. Mathematical theory of heat distribution during welding and cutting. Weld J 1941;20.

[42] Rosenthal D. The Theory of Moving Sources of Heat and Its Application of Metal Treatments. Trans ASME 1946;68:849–66.

[43] Van Elsen M, Baelmans M, Mercelis P, Kruth JP. Solutions for modelling moving heat sources in a

semi-infinite medium and applications to laser material processing. Int J Heat Mass Transf 2007;50:4872–82. doi:10.1016/j.ijheatmasstransfer.2007.02.044.

[44] Tan H, Chen J, Zhang F, Lin X, Huang W. Process analysis for laser solid forming of thin-wall structure. Int J Mach Tools Manuf 2010;50:1–8. doi:10.1016/j.ijmachtools.2009.10.003.

[45] Ning J, Sievers D, Garmestani H, Liang S. Analytical Modeling of In-Process Temperature in Powder Bed Additive Manufacturing Considering Laser Power Absorption, Latent Heat, Scanning Strategy, and Powder Packing. Materials (Basel) 2019;12:808. doi:10.3390/ma12050808.

[46] Dowden J. Why Construct Analytical Models Of Laser Welding? AIP Conf. Proc., vol. 1047, 2008, p. 3–11.

[47] Gellert B, Egli W. Melting of copper by an intense and pulsed heat source. J Phys D Appl Phys 1988;21:1721–6. doi:10.1088/0022-3727/21/12/009.

[48] Dowden JM. The mathematics of thermal modeling: an introduction to the theory of laser material processing. CRC Press; 2001.

[49] Steen WM, J. M. Laser Material Processing. vol. 1. 2010. doi:10.1007/978-1-84996-062-5.

[50] Hess A, Schuster R, Heider A, Weber R, Graf T. Continuous wave laser welding of copper with combined beams at wavelengths of 1030nm and of 515nm. Phys Procedia 2011;12:88–94.

[51] Demir AG, Previtali B. Laser Metal Deposition Employing Scanning Optics 2017;0:1–20.

[52] Dowden JM. Mathematics Modeling Theory of Laser Material Processing. 2001.

[53] Singh SS, Roy D, Mitra R, Subba Rao R V., Dayal RK, Raj B, et al. Studies on laser sintering of mechanically alloyed Al50Ti40Si10 composite. Mater Sci Eng A 2009;501:242–7. doi:10.1016/j.msea.2008.10.011.

[54] Franco A, Lanzetta M, Romoli L. Experimental analysis of selective laser sintering of polyamide powders: An energy perspective. J Clean Prod 2010;18:1722–30. doi:10.1016/j.jclepro.2010.07.018.

## List of figures



## List of tables